

**Counter-current flow limitation for air-water and steam-water flows in a  
PWR-relevant geometry**

Lucas, D.; Beyer, M.; Pietruske, H.; Szalinski, L.;

Originally published:

August 2017

**Nuclear Engineering and Design 323(2017), 56-67**

DOI: <https://doi.org/10.1016/j.nucengdes.2017.07.032>

Perma-Link to Publication Repository of HZDR:

<https://www.hzdr.de/publications/Publ-25404>

Release of the secondary publication  
on the basis of the German Copyright Law § 38 Section 4.

CC BY-NC-ND

# **Counter-current flow limitation for air-water and steam-water flows in a PWR-relevant geometry**

D. Lucas, M. Beyer, H. Pietruske, L. Szalinski

## **Abstract**

Steady state counter-current flow limitation (CCFL) experiments were conducted in a 1:3 scaled flat model of the hot leg and part of the steam generator inlet chamber of a German Konvoi pressurized water reactor. The experiments include air-water tests at 1 and 2 bar as well as steam-water tests at 10, 25 and 50 bar. Flooding characteristics are obtained in dependency on the dimensionless gas and liquid flow rates (Wallis-parameter). They should a slight, but clear dependency on pressure – with increasing pressure more liquid can flow in counter-current to the gas in case of partial CCFL. Also the dimensionless gas flow rate for zero penetration slightly increases with pressure. Beside the flooding characteristics also slug frequencies were analyses basing on pressure measurements along the horizontal part of the test section. Finally, comprehensive video material was obtained which is suited for extracting quantitative data on the local flow structure. This can contribute to the further CFD-code development and validation.

## **1. Introduction**

The counter-current flow limitation (CCFL) phenomenon is relevant in several accident scenarios for nuclear power plants. In the event of a loss-of-coolant-accident (LOCA) it is necessary to guarantee a safe removal of the decay-heat after shut-down of the reactor. During such an accident the coolant inventory of the primary loop leaks out and in a pressurized water reactor (PWR) the pressure decreases down to saturation conditions. The evaporation then stabilizes the pressure and two-phase flow occurs in the primary circuit. Combined with assumptions on failures of safety devices such as

high pressure emergency core cooling injection systems the level in the reactor pressure vessel (RPV) may decrease. Thus, a situation may occur in which the main circulation pipes are partly or completely free of coolant. In this case a natural circulation is expected in which the steam produced in the reactor core flows along the hot leg pipe into the steam generator (SG). There it condenses and parts of the condensate flow back via the hot leg to the reactor core. This so-called reflux-condenser mode (Wang & Mayinger, 1995) is schematically shown in Fig. 1. It contributes to the core cooling and is a part of the safety strategies for PWRs.

A slightly different situation leading to the reflux-condenser mode is discussed by Nariai et al. (2010). During a PWR plant outage for maintenance or refueling, the level of the primary coolant is to be kept in the center of a hot leg and the reactor coolant is cooled by a residual heat removal (RHR) system. This operation is called “mid-loop operation”. In case of a failure of the RHR system the reflux-condenser mode is one of the possible measures to retain the cooling of the core.

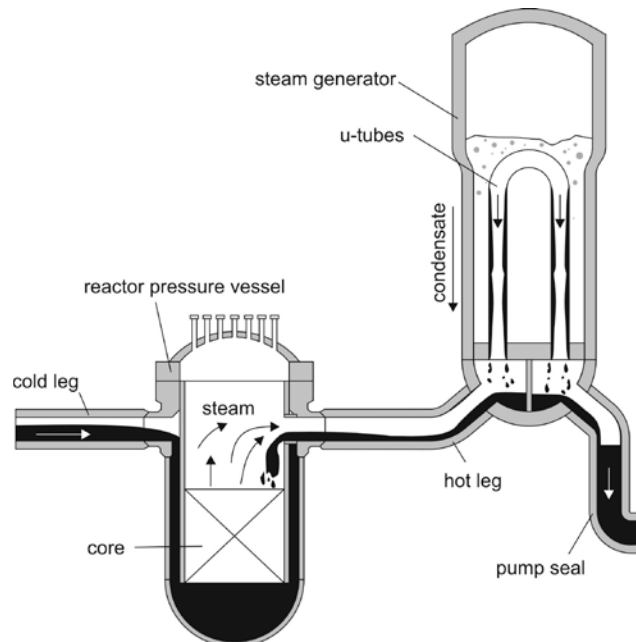


Fig. 1: Scheme of the reflux-condenser mode

However, in both scenarios the stratified counter-current flow of condensate and steam is only stable for a certain range of flow rates (Bankoff & Lee, 1986). If the steam flow rate exceeds this limit, for example due to the unavailability of the steam generator of another loop, the condensate can be clogged in the hot leg. This is the beginning of the counter-current flow limitation: the liquid is carried over by the steam and partially entrained in opposite direction to the steam generator. As a consequence, the hot leg and steam generator are flooded, which further decreases the water level in the RPV and, therefore, deteriorates the core cooling (Vallée et al. 2012). In case of a further increase of the steam flow rate, the condensate flow towards the RPV could be completely stopped (zero penetration). Detailed examples of such LOCA scenarios leading to the reflux condenser mode as well as to CCFL are described by Jeong (2002).

Many different experiments were done to investigate the CCFL phenomenon related to the PWR configuration. Examples are the large scale experiments by Weiss and Hertlein (1988) or Mayinger et al. (1993), scaled down experiments by Richter et al. (1978), Wongwises (1996), Minami et al. (2008), Vallée et al. (2012), Al Issa and Marcian (2014) and Ohnuki et al. (1988) who discussed scale effects. These experiments cover different scales as well as different fluid systems (Deendarlianto et al., 2011). Wallis and Dobson (1973) introduced the non-dimensional superficial velocity  $j_k^*$  (well-known as Wallis parameter) defined by:

$$j_k^* = \frac{j_k}{\sqrt{g \cdot D}} \sqrt{\frac{\rho_k}{\rho_L - \rho_G}} \quad (1)$$

with  $j_k$  as the superficial velocity of the phase  $k$ ,  $g$  – the acceleration of gravity,  $D$  – the pipe diameter and  $\rho$  the density. The index  $k$  stands for the phase,  $L$  – for liquid and  $G$  – for gas. CCFL can be characterized by flooding curves which means plots of  $j_G^*$  over  $j_L^*$ .

From comparisons of such plots between air-water and steam-water experiments Ohnuki (1986) concluded that no essential differences can be observed in the CCFL

characteristics of air-water and steam-water systems. However, from all these studies different correlations on flooding curves were obtained and many open questions remained. A review on the CCFL phenomenon related to nuclear safety including a detailed discussion on the experiments can be found in Al Issa and Macian (2011).

For accident analyses the use of one-dimensional system codes is state of the art. The CCFL phenomenon is considered in such codes based on empirical correlations. Such correlations which were obtained by the above mentioned experiments cannot simulate CCFL on first principle fluid dynamics models and are valid only for specific geometries and scales. However, CCFL is connected with very complex 3D flow structures. In principle computational fluid dynamics (CFD) methods can handle such flows, but especially for complex two-phase flows they presently are not yet mature and do not meet the high level of confidence needed in the field of nuclear reactor safety (Lucas et al., 2016). Moreover, the developed models and closure laws embedded in CFD must be validated to allow reliable simulations. Therefore, high-resolution experimental data at reactor typical boundary conditions is needed for comparison with CFD calculations.

Motivated by this fact an experiment was built up at Helmholtz-Zentrum Dresden – Rossendorf several years ago. In contrast to previous experiments which aimed mostly on the development of correlations for system codes more detailed insights in the flow structure and CFD-grade data were expected. For this reason a flat geometry representing a central cut of the hot leg and SG inlet chamber of a German Konvoi PWR was considered. This so-called “hot leg model” was installed in the pressure chamber of the TOPFLOW (Transient two Phase FLOW) test facility of Helmholtz-Zentrum Dresden Rossendorf (HZDR). Beside experiments on co-current and counter-current flow also CCFL experiments were performed with air-water as well as with steam-water at pressures of up to 50 bar (Vallée et al., 2012). In their conclusions Vallée et al (2012) summarize: “A comparison between the air/water and steam/water flooding curves first revealed a difference when plotted in terms of the classical Wallis parameter or Kutateladze number. Further investigations show that the steam was probably wet, which requires a correction of the steam measurements. The amount of parasitic water was evaluated indirectly over the zero liquid penetration noticed in the CCFL diagram.

Finally, the experimental results confirm that the Wallis similarity is appropriate to scale flooding in the hot leg of a PWR irrespective of the gas (air or steam) and for pressures ranging from 1.5 to 50 bar and temperatures of 18 to 264 °C. However, the assumptions made for data correction unfortunately could not be conclusively confirmed from the available data. Furthermore, it was not possible to determine the exact origin of the parasitic water due to lack of specific instrumentation. Plausibility checks show that the amount of liquid cannot only be explained by heat losses and is probably also due to liquid entrainment from the separator of the TOPFLOW heater circuit. Consequently, uncertainties remain in the adapted method to correct the results, which should be clarified in a second experimental campaign.”

The data obtained by these experiments were extensively used for CFD-model development and validation (e.g. Deendarlianto et al., 2011, 2012, Kinoshita et al., 2012, 2014). It turned out that the experiments are quite useful for this purpose, however, due to the fact that the experiments were done transient with a stepwise increase of the gas flow rate, long simulation times were required. Here steady state CCFL-conditions could be helpful for further simulations.

For these reasons, basing on the experiences gained with the first test series now new tests were done. A completely new test rig was built up maintaining the basic geometry of the test section itself. This paper reports on the new experiments and the results obtained.

## **2. CCFL experiments**

As in previous experiments (Vallée et al., 2012) a model of a German PWR of the Konvoi type was chosen. The CCFL may appear in the hot leg and in the SG inlet chamber. Accordingly, these parts of the primary circuitry were modelled in a scale of 1:3. In order to provide optimal observation possibilities, the circular pipes were replaced by a flat, 50 mm wide geometry. To enable beside air-water also steam-water experiments at pressure values up to 50 bar the test rig was operated in the TOPFLOW

pressure chamber. This is a tank with an inner diameter of 2.44 m and an inner length of 7.24 m which serves as a container for the test rig. It can be operated at pressures up to 50 bar and an inner temperature up to 70 °C. However, due to measuring technique which is installed inside the tank it was defined that the temperature of the tank atmosphere should not exceed 50 °C. This is achieved by a cooling system with a maximal power of 30 kW. In addition a thermal insulation of the test section and built-in condenser is required.

The tank can be pressurized with nitrogen up to the above mentioned maximum pressure. This allows to achieve a pressure equilibrium inside and outside the test section. During operation with steam-water non-condensed steam flows from the test rig into the upper end of a vertical high pressure condenser. This condenser is connected from the lower end to the tank atmosphere and separates the steam inside the test section from the gas tank atmosphere. Due to the density difference between steam and gas a stable stratification appears. The level of the separation layer depends on the received steam mass flow respectively the condensation power. A shift of the level increases or decreases the length of the vertical cooling pipes which is available for steam condensation. Accordingly the system is self-regulating. The reliable operation of this technique was verified in several experiments that used this technology.

## **2.1 Test section**

A schema of the new designed test section is shown in Fig. 2. The main components are: the RPV simulator tank, the horizontal part of the hot leg, inclined model of the SG inlet chamber and SG separator tank. To enable steady state CCFL experiments the SG separator tank is divided into two parts by a steel sheet. The water is injected into the inner one (B20A in Fig. 2, cross section 300 x 400 mm<sup>2</sup>) which is connected directly to the SG inlet chamber; the outer one (B20B in Fig. 2, cross section 600 x 800 mm<sup>2</sup>, height 1650 mm) is used as a water drain. As soon as CCFL occurs not all of the water injected into B20A can flow towards the RPV simulator, but is pushed back by the steam flow. For steady state operation this water has to be drained off from the SG separator.

To keep the level in B20A constant the steel sheet serves as level drain. Thereby the height of the steel sheet was set to the upper bend of the inclined test section part (1097 mm). The excess water flows into the B20B tank and is withdrawn from its bottom. A perforated plate at the top of the tank avoids that water drops flow to the condenser in case of churn flow.

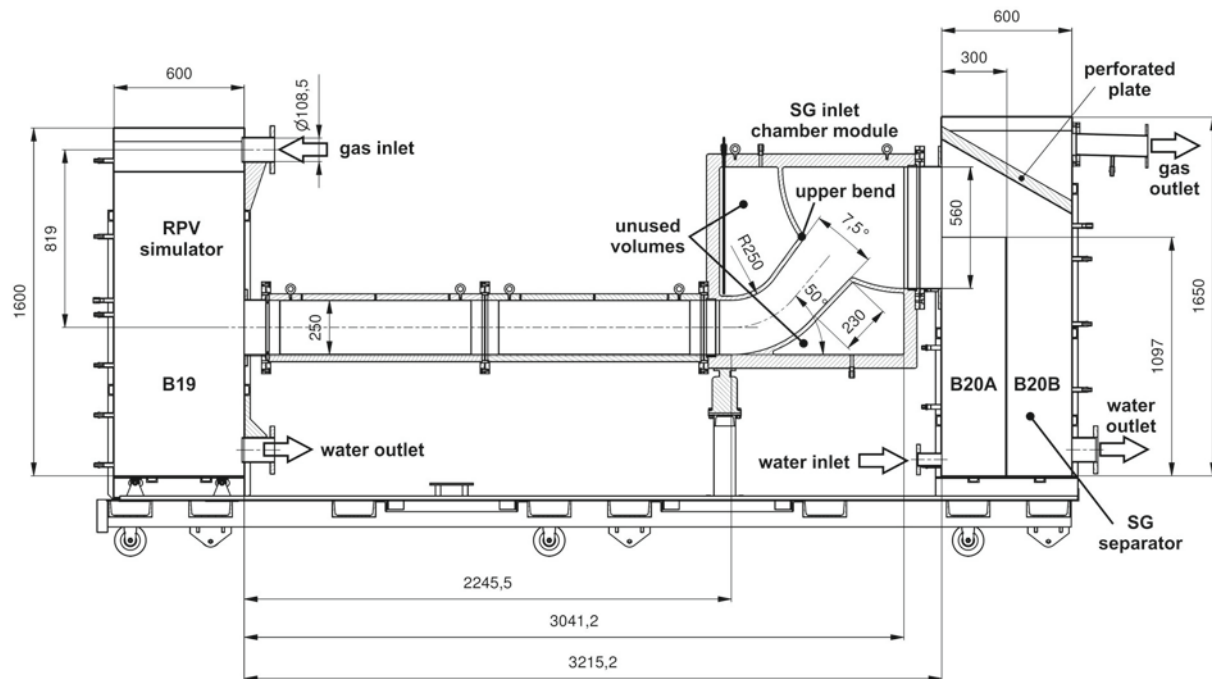


Fig. 2: Central cut through the mid-plane of the test section

The RPV simulator is on the left side at Fig. 2. It feeds the hot leg with gas and receives water flow from the channel. The top part of the tank is equipped with a standard perforated plate, to allow an almost uniform gas distribution. The dimensions of the tank are similar to the SG separator (600 x 800 x 1600 mm<sup>3</sup>).

The horizontal part of the hot leg has a thickness of 50 mm, a height of 250 mm and a total length of 2245.5 mm. The geometry of the SG inlet chamber module is more complex and the details are shown in Fig. 2. The thickness of this part is also 50 mm.

Since accurate mass balances are important for the CCFL-experiments the inner volumes of the tanks and the channel were designed with smooth walls and without inner stiffing details. The test section parts and both tanks are connected among each other by rectangular flanges with graphite seals and bolts. All connections, inner areas and details were designed and manufactured in consideration of high quality standards, small deviations and tolerances, to avoid flow disturbances.

The CCFL test rig was erected at a moveable platform. While the SG separator was fixed permanently, the test section and the RPV simulator were mounted to be movable, in order to compensate the thermal elongation during operation.

The horizontal part of the hot leg as well as the SG inlet chamber module allow an optical observation of the flow by glass windows. For the SG inlet chamber module rectangular glass panes with the dimension 889 x 874 mm<sup>2</sup> are mounted on separate steel frames – see Figs. 2 and 3. These frames are mounted to the basic module by bolted assembling and tightened by graphite seals. The unused volumes are opened to the tank atmosphere to avoid stresses by pressure changes and thermal expansion of entrapped gas. For the horizontal part of the hot leg four (two on both sides of the channel) rectangular glass windows each with the dimensions 901 x 268 mm<sup>2</sup> were used.

The test section is operated at high temperatures and in addition to the above mentioned cooling circuit of the pressure chamber an effective thermal insulation of the test section is required. Metal sheets and pipes can be covered by insulating materials, but the observation requires transparent windows for picture recording and illumination.

The non-transparent areas are insulated by covering it with plates or blankets of pure inorganic and open porous material. Planar areas are covered with plates of Multitherm 550. Stainless steel sheets are used to protect the insulation from humidity and mechanical damage. For insulation of curved areas (pipes, flanges) a similar material is used, but it is manufactured as blanket (Superwool SW 607 blanket 128). To avoid gas

diffusion through the insulation packings, between each layer a very thin stainless steel foil (50  $\mu\text{m}$ ) is added. Normally complete pipe insulation consists of 4 – 6 layers and is protected by a steel foil. Both insulation techniques allow pressure equalization to endure pressure changing of the ambient gas atmosphere.

For the observation windows a package of glass windows is assembled in such a way that some identical glass panes are put on each other. Between the panes PTFE tape is placed at the circumference. Thus, closed gas volumes form that serve as thermal insulation. A hole in the PTFE tape at bottom position of the glass package allows pressure equalization. Fig. 3 shows the SG inlet chamber module with complete insulation. Here a package of 4 glass panes is applied that is mounted directly to the inner temperature proof glass window and assembled by steel outriggers. Around the glass package the thermal insulation is made from Multitherm 550 with a final steel protection layer. At the left side in the middle part of Fig. 3 two thermocouples are shown. They were used to monitor the temperature in the inner gap and at the outer side of the glass package. While the inner proof glass pane has a thickness of 15 mm, the glass panes of the package are thinner (5 mm). Both types were made from Borofloat 33 glass, manufactured by the German company Schott. The glass packages of the horizontal test section modules are prepared in a similar way. More details on the insulation concept can be found in the experimental report by Beyer et al. (2016).



Fig. 3: Thermal insulation of the SG inlet chamber module

## 2.2 Measurement techniques and data evaluation

For the CCFL-experiments extensive operational measuring technique for mass or volume flow rates, temperature, pressure and differential pressure are available as illustrated in Fig. 4. The figure shows the position of the sensors. The type of sensor is marked by 1<sup>st</sup> letter: T – temperature, P – pressure, PD – differential pressure, L – level, E – electrical parameter (voltage, current, power), F – mass- or volume flow, Q – concentration or thermal power. These sensors are used to control the experiment, to guarantee a safe operation and to obtain data. Here only the most important measurements and procedures to obtain the experimental data presented in section 3 are outlined. For further details please check the experimental report by Beyer et al. (2016). This report also includes the complete information on calibration procedures and on the accuracy of the single sensors.



which are part of the documentation. Once the corrected volume flow rate in the test section is available the superficial velocity can be calculated by:

$$j_G = \frac{\dot{V}_{G,TS}}{A_{ch}} \quad (2)$$

Here  $\dot{V}_{G,TS}$  is gas volume flow rate in the test section and  $A_{ch}$  is the cross section of the horizontal part of the hot leg (50 x 250 mm<sup>2</sup>).

The second parameter to quantify for the flooding characteristics is the liquid flow rate discharged to the RPV simulator. The water is circulated in closed loops. It is withdrawn from the RPV simulator tank B19 by pump P18 and the outer tank of the SG separator B20B by pump P16 and injected into the inner SG separator tank B20A. The flow rates are measured separately for each pump lines by Coriolis flow meters. Additionally the injected water volume flow rate is adjusted basing on a third flow meter. Thus, the flow discharged to the RPV simulator can be determined directly by a balance for the flow rate water withdrawn from the RPV simulator and the level change in the same tank as indirectly by a similar balance for the outer SG separator tank. To get the exact balances level changes in both tanks as well as local temperatures have to be included into the consideration. The water levels in the tanks are determined by measurements of the pressure difference long the tank height. For steam water flow additional corrections considering condensation effects based on estimated heat losses are done. Again the sophisticated procedure is documented in the experimental report by Beyer et al. (2016) and can be reproduced via Excel-sheets which are part of the documentation. The corresponding superficial water velocity is calculated in analogy to gas by:

$$j_L = \frac{\dot{V}_{TS}^{dis}}{A_{ch}} \quad (3)$$

with the volume flow rate discharged to the RPV simulator  $\dot{V}_{TS}^{dis}$ .

Basing on gas and liquid superficial velocities and the densities based on local temperature and pressure the Wallis-parameter can be calculated:

$$j_k^* = \frac{j_k}{\sqrt{g \cdot H}} \sqrt{\frac{\rho_{k,TS}}{\rho_{L,TS} - \rho_{G,TS}}} \quad (4)$$

Here  $j_k$  is the superficial velocity of the phase  $k$ ,  $g$  – the acceleration of gravity,  $H$  – the channel height and  $\rho$  the density. The index  $k$  stands for the variable phase,  $L$  – for liquid and  $G$  – for gas while the index  $TS$  refers to the test section conditions. With these parameters the CCFL-characteristics are analyzed. The results are discussed in section 3.

In order to obtain information on the slug behavior 6 pressure sensors were installed at the horizontal test section module. Their measurement positions are almost equally distributed along the channel length at the top of the horizontal channel. While the TOPFLOW data acquisition system stores the parameter with a frequency of 1 Hz these pressure data were measured with a frequency of 10 Hz. Slug frequencies are determined based on these pressure sensors by a fast Fourier transformation (FFT). Fig. 5 shows 2 plots of characteristic FFT-pattern. At the left side a clear spectrum is visible. In this case the maximum rate of occurrence represents the most probably frequency, whereat some further maxima exist. In opposite the right graphic shows a much more expanded spectrum. Here the maximum rate of occurrence results in a random frequency. Most of the FFT data belong to the second class. For this reason a weighted averaging method was applied on all data to obtain the characteristic frequency. First an averaged value of the occurrences is determined. It is represented by the dotted lines in Fig. 5. The characteristic frequency was determined as weighted average of the region of the spectrum in which values larger than this threshold occur. Since this region may be influenced by random occurrences which exceed this threshold, the threshold was increased by a factor of 1.8 before the region for the weighted averaging was defined. In Fig. 5 this new threshold is shown by the solid black line. The factor 1.8 was determined to obtain results which show a minimum sensitivity on this value. The resulting weighted frequency is shown in both graphs as green

vertical line. These values are the basis for the analysis of slug frequencies presented in section 3.

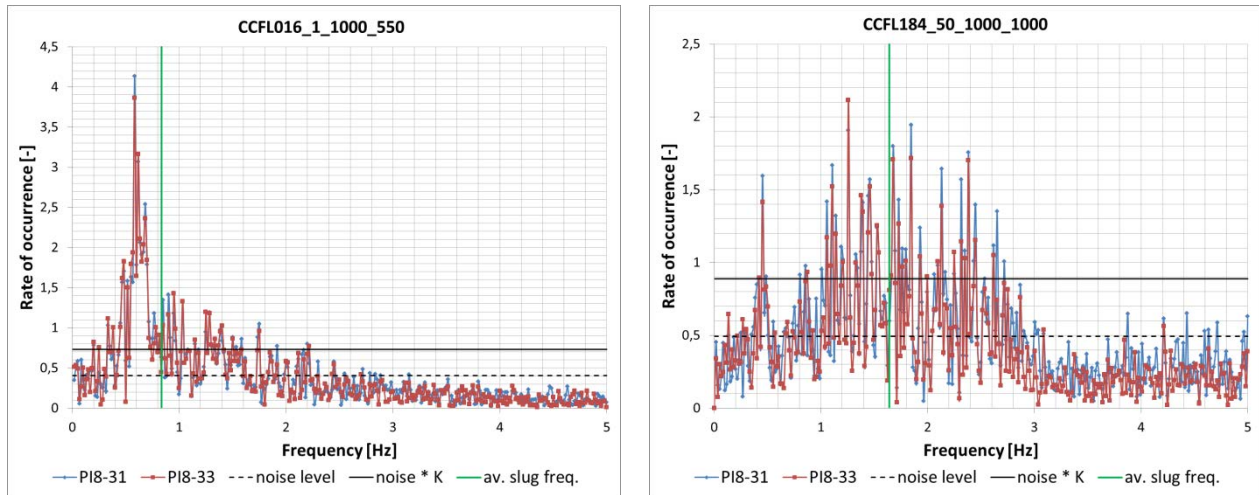


Fig. 5 FFT data for two selected hot leg tests: left side – air water test 016 at 1 bar pressure and 558 nm<sup>3</sup>/h gas flow; right side – steam water test 184 at 50 bar pressure and 967 g/s steam mass flow; both tests with 1 kg/s injected water mass flow

As mentioned above the TOPFLOW pressure chamber technology allows to conduct the experiment under pressure equilibrium inside and outside the test section. The main advantage is the possibility to apply optical measurement techniques and high speed video camera observations via the glass windows described above. This allows to obtain detailed information on the flow structure from video cameras. For the horizontal part two web cams were applied. To observe the entire length of the channel without a mirror system each camera was equipped with a wide-angle lens with a fixed aperture. To avoid the wide-angle picture distortion as much as possible, the middle plane of the lens was adjusted to the bottom edge of the horizontal channel. So the image section of interest, i.e. a long small stripe, was recorded in an acceptable quality. During the CCFL picture sequences were recorded with a frequency of 60 Hz and an image size of 1280 x 720 pixels. The flow behavior in the inclined module is more turbulent and has to be observed with a higher frequency. A high speed camera with a progressive CMOS (8 μm pixel size) was used. It is very light sensitive up to ISO 3200 on monochrome modus. During the current tests the CCFL high speed picture sequences were recorded with an image size of 1250 x 1250 pixels and a frame rate of 500 fps for 13 s, so that 6500 single images used the available camera memory of 10 GByte to full capacity.

The cameras were installed inside the TOPFLOW pressure tank. Since commercial non-pressure-proofed devices were applied, they have to be protected from damage by installation in pressure-proof boxes. The last one are designed as cylindrical one-side closed containers with an observation window at the front side that may be opened for installation and service purposes. During operation the cameras produce heat that is removed from the containers to the ambience by air flushing. For illumination LED panels with 70 single LED's were used. 12 LED-panels were equally distributed parallel to the glass window and assembled to a holding frame at the SG inlet chamber module. While the distance between the panels and a diffuser plate was determined as 50 mm, the diffuser plate is about 100 mm away from the outer insulation glass pane. This configuration was found as an optimum for a homogeneous illumination. The smaller windows at the horizontal test section modules were illuminated by 3 panels each in a similar way.

### **2.3 Experimental procedure and test matrix**

All experiments were conducted in the closed TOPFLOW pressure chamber. Different procedures are required to prepare the air-water and the steam-water experiments, respectively. They are presented in detail in the experimental report by Beyer et al. (2016). Here only the most important information is given.

The thermal hydraulic boundary conditions for the measurements should be chosen to cover the whole range of CCFL flow conditions from onset of flooding until zero penetration. Some experiences obtained during previous CCFL-experiments by Vallée et al. (2012) could be used, however, due to the fact that these experiments were done at transient CCFL conditions, while now steady state conditions were aspired, this regions had to be determined again. In previous experiments injected water flow rates between 0.3 kg/s and 0.9 kg/s were used. Higher water flow rates were not feasible for CCFL-conditions, since they would have led to too much accumulation of water in the SG simulator tank. Basing on these experiences it was defined to do experiments with water flow rates of 0.3, 1.0 and 2.0 kg/s. After the definition of the injected water mass

flows, pretests with air and water at ambient pressure were carried out to define the new gas flow limits. This information was used to prepare the test matrix for cold air-water flows. Then these tests were completed and the results were used to calculate the new flooding characteristic in terms of Wallis parameter. On this basis the CCFL steam mass flows were defined in consideration of the pressure levels that led to the thermal hydraulic parameters for the steam-water matrix. Finally a second air-water series was scheduled to investigate the flooding characteristic for a doubled pressure level of 2 bar.

The resulting test matrices for air-water and steam-water experiments are shown in Tab. 1 and Tab. 2, respectively. The experiments are arranged according to pressure and water mass flow. The columns include pairs of unique test numbers and associated gas volume flow rates. Each column groups the single tests to one series, starting with an unlimited counter-current flow (green colored), as next tests with increasing gas flow (CCFL) up to zero penetration (blue labeled) and further with decreasing gas flow down to the collapse of CCFL. Finally again a flow test on counter-current flow without limitation (again marked green) completes the series. It should be mentioned that the test series for a given pressure and injected liquid mass flow rate were done in the same order as shown in one column of the test matrix – i.e. starting with low gas flow rate, stepwise increase of the gas flow rate until zero penetration was reached and subsequent stepwise decrease of the gas flow rate. For the single steps of gas flow rates steady state conditions were reached by keeping the operational parameters for that state constant during a minimal period of 10 minutes after achieving all aspired parameters. The steps for the increase and decrease of the gas flow rates were chosen to obtain enough data on flooding characteristics on the one hand, but also to limit the experimental costs on the other. Some tests were repeated for reproducibility (e.g. 46b and 47b).

The gas flows in both matrixes are corrected values. So, the norm air flow was adjusted in consideration of the results of the post measurement re-examination of the air flow meters FIC4-11 and FIC4-10 (see Beyer et al., 2016 for details). The steam mass flow was corrected in accordance to the heat losses in the steam pipe and to the results of energy and mass balances in the test rig as well as in the condenser.

Tab. 1: Test matrix for the air-water CCFL tests

Pressure [bar]	1						2			
Water mass flow [kg/s]	2		1		0.3		2		1	
Test number / Gas volume flow [m <sup>3</sup> /h] norm			11	432.8					230	574.7
			12	442.0					231	625.7
	1	484.2	13	471.8	23	483.5			232	706.6
	2	508.5	14	506.7	24	506.6	210	808.2	233	757.6
	3	608.3	15	608.3	25	607.5	211	879.3	234	828.3
	4	556.8	16	557.5	26	557.1	212	777.8	235	737.8
	5	506.3	17	506.4	27	506.5	213	717.3	236	686.5
	6	458.9	18	459.2	28	488.3	214	656.0	237a	635.5
	7	414.4	19	414.4	29	476.0	215	574.5	237b	635.6
	8	313.5	20	366.2	30	467.5	216	498.4	238	584.6
	9	258.6	21	356.1			217	458.0	239	544.0
	10	246.8	22	345.7			218	413.6	240	513.6
						219	364.8	241	492.1	

Tab. 2 Test matrix for the steam-water CCFL tests

Pressure [bar]	10						25						50			
Water mass flow [kg/s]	2		1		0.3		2		1		0.3		2		1	
Test number / Steam mass flow [g/s]									120	535					180	683
			60	297	80	346			121	577					181	738
			61	355	81	384	100	580	122	636	140	553	160	687	182	801
	40	329	62	391	82	420	101	672	123	692	141	626	161	879	183	848
	41	447	63	448	83	479	102	741	124	764	142	806	162	1050	184	967
	42	410	64	411	84	393	103	615	125	664	143	603	163	838	185	889
	43	373	65	377	85	372	104	545	126	603	144	586	164	772	186	823
	44	333	66	326	86	349	105	492	127	533	145	570	165	704	187	760
	45	294	67	280			106	430	128	491			166	635	188	698
	46a	254					107	372	129	469			167	574	189	658
	46b	257					108	323	130	417			168	514	190	608
	47a	217											169	477		
	47b	212											170	417		

After the above mentioned waiting time of 10 minutes the single measurement was started by activating of the image recording of both web cams which capture the horizontal part of the hot leg. After this, the high-speed camera, two indicator LEDs for

the web-cams and the data logger of the special pressure sensors were triggered. Thereby the high-speed camera captured images for 13 s, the web cam LEDs glowed for 60 s and the pressure signals were recorded with the 10 Hz frequency also for 60 s. Only for the first 3 air-water tests at 1 bar the capturing time for web cams and pressure sensors was 30 s. After completion of the triggering the web cams were switched off, the gas volume flow was changed to the next matrix point and the measurement procedure starts again.

In case of counter-current flow without limitation of the liquid flow towards the RPV simulator only the pump P18 (see Fig. 2) was operated – i.e. all the water injected into the SG separator tank was withdrawn from the RPV simulator tank. As long as the water level in this tank remained constant no CCFL occurred. For an increased gas flow the CCFL started and the water flow from the SG separator to the RPV simulator was obstructed (onset of flooding). This effect led to water retention in the SG separator tank B20A and hence to a level increase and finally to a water flow over the steel sheet in the B20B tank. To control the water balance in the RPV simulator B19 and the SG separator B20B tanks the pumps P16 and P18 (see Fig. 2) were used together. The pump flow rates were adjusted in accordance with the obstruction level of the CCFL. In case of zero-penetration all the water injected into the inner SG separator tank (B20A) was withdrawn from the outer SG separator tank (B20B). The constant levels in tanks B19 and B20B indicated that no water flows in counter-current to the steam along the test section. Additionally the zero penetration was identified by the optical observation as shown in Fig. 6. During complete CCFL the channel part near the RPV simulator was free of water (red oval).

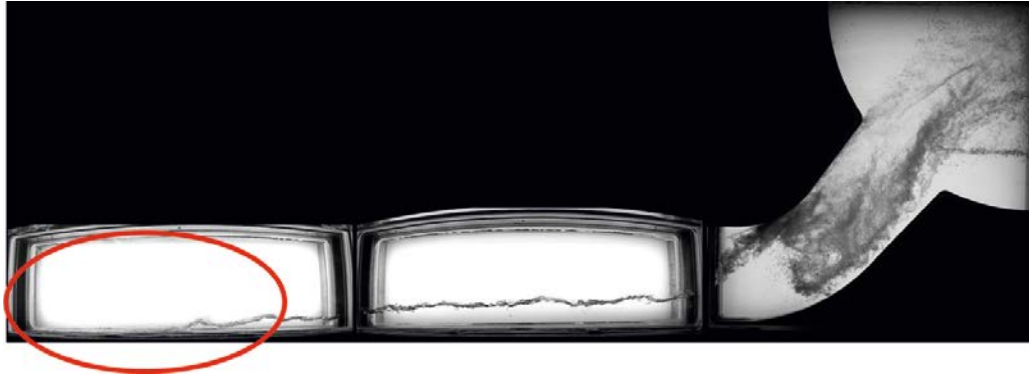


Fig. 6 Photo composition of synchronous images of all 3 cameras, matrix point 162: 50 bar steam-water test with 2 kg/s injected water- and 1.05 kg/s steam mass flow, zero penetration condition

### 3. Results

First results are already implied in the test matrices Tab. 1 and Tab. 2. The green marked values for inset of flooding and breakdown of flooding show the well-known hysteresis of the CCFL phenomenon. The CCFL starts at significantly higher gas flow rates during increasing gas flow and it remains down to lower flow rates in case of decreasing gas flow. The width of this hysteresis depends on the injected water mass flow, as higher the water flow as wider the hysteresis. This fact is easy to understand, because as higher the injected water mass flow as more liquid is available above the inclined test section module and can feed the discharge water flow. Also a second effect can be directly seen from the test matrices: for all series with 1 kg/s injected water mass flow the CCFL starts earlier than for the series with more (2 kg/s) or less (0.3 kg/s) injected water flows. The reason for this effect is not yet clear. The corresponding test series are visualized in Fig. 7. The figure shows all CCFL test series starting from the counter-current flow, down to zero penetration condition and back to the counter-current flow without limitation.

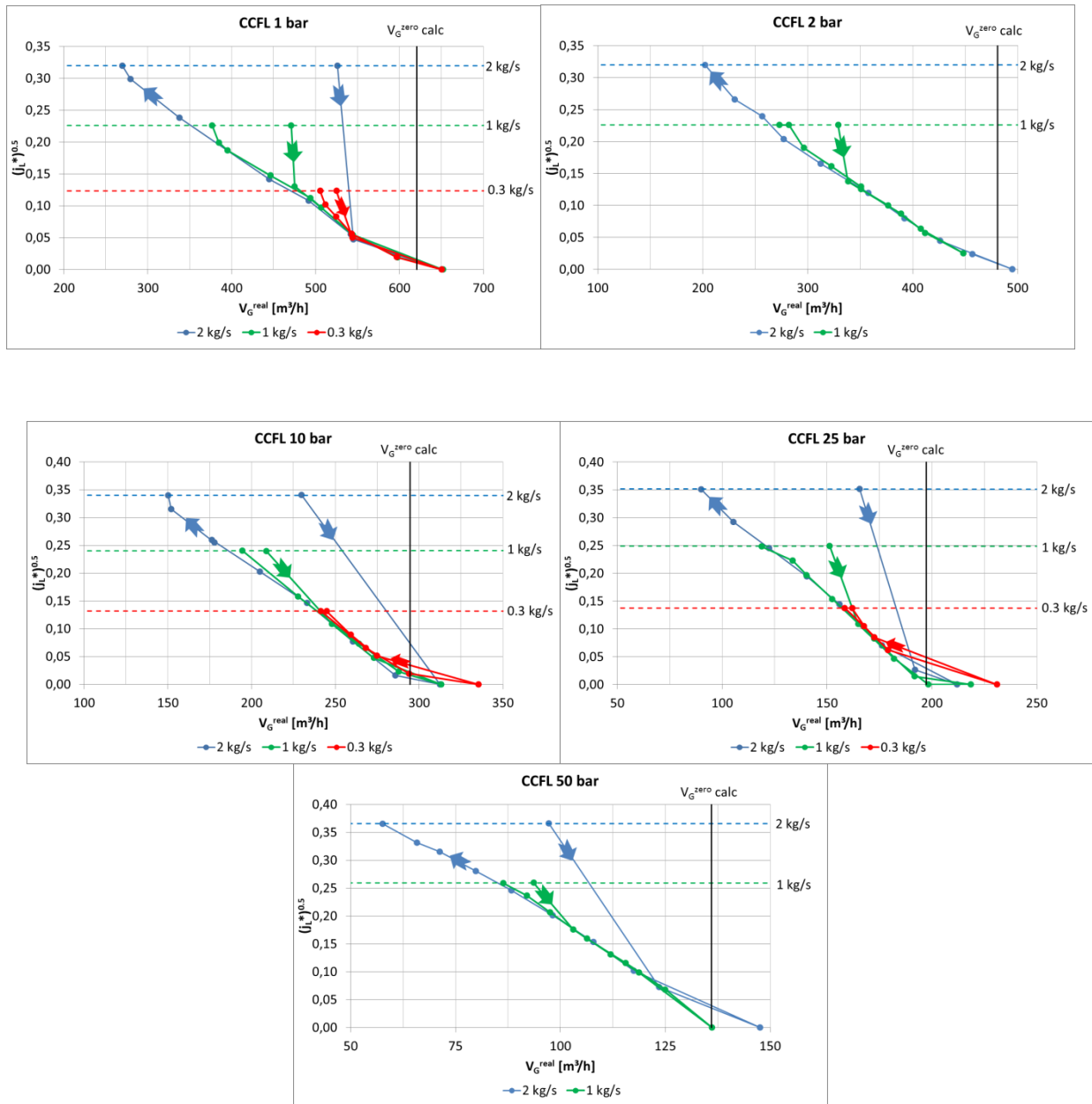


Fig. 7 CCFL test series development sorted by pressure and injected water mass flow

The flooding characteristics basing on the dimensionless flow rate (Wallis-Parameter) is shown in the usual way (gas flow rater over discharged liquid flow rate) in Fig. 8. It displays the tests of the flooding and de-flooding measurements that are arranged at the same line. The air-water tests at 1 bar marked with blue and the 2 bar tests with black symbols. For the visualization of the steam-water results the following colors were used: 10 bar: green, 25 bar: yellow and 50 bar: red. Further the rhombs mark the tests with 2

kg/s water injection, the quadrats – 1 kg/s and the triangles – 0.3 kg/s respectively. So the graph shows the tests arranged by series according to the columns in Tab. 1 and Tab. 2. It is clearly visible, that for the single series, started with 1 bar air tests, the non-dimensional gas superficial velocity increases with increasing pressure for constant discharged liquid flow, i.e. there is a slight dependency on material parameters which is not reflected by the Wallis parameter. Furthermore the test points form almost straight lines for each pressure and are independent of the injected water mass flow.

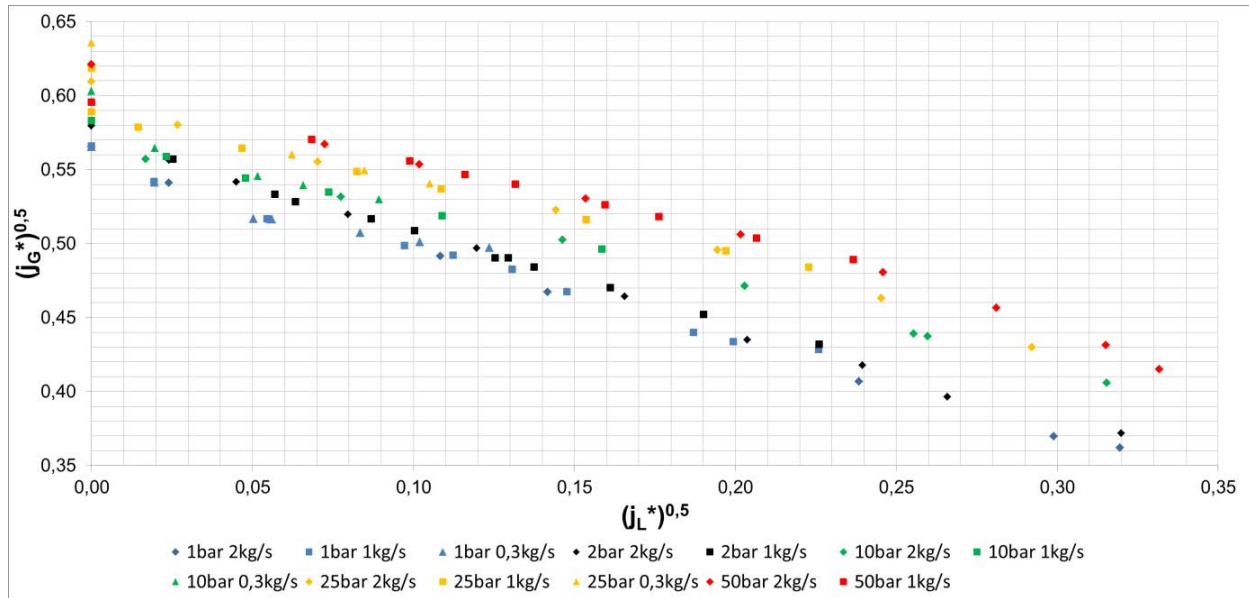


Fig. 8 Flooding characteristics of the hot leg model plotted in terms of Wallis parameter

For a further analysis the linearity of the curves of the single series was investigated in detail. Due to the fact, that the test points with zero discharged liquid flow have mostly an increased gas flow (defined by the step of the gas flow rate – which more or less exceeds the exact minimum gas flow rate leading to zero penetration), these points are eliminated from the linearity check. Fig. 9 exemplary shows the data for all three 10 bar steam water test series with linear fits on the left side and quadratic approximation on the right side for the 2 kg/s series. Similar to these graphs all data were processed and the results are summarized in Tab. 3. Beside the pressure and the injected liquid mass flow it contains the parameters of the fitting procedure: P2 as quadratic, P1 as linear and P0 as absolute value. P2 only exists for the 2 kg/s series because only in this case and only for the steam tests a quadratic approximation results in a significant improvement of

the fit, e.g in a significant reduction of the coefficient of determination ( $R^2$ ). For the other experiments the test points are arranged more or less in a stochastic way. Hence the linear fit seems to be sufficient.

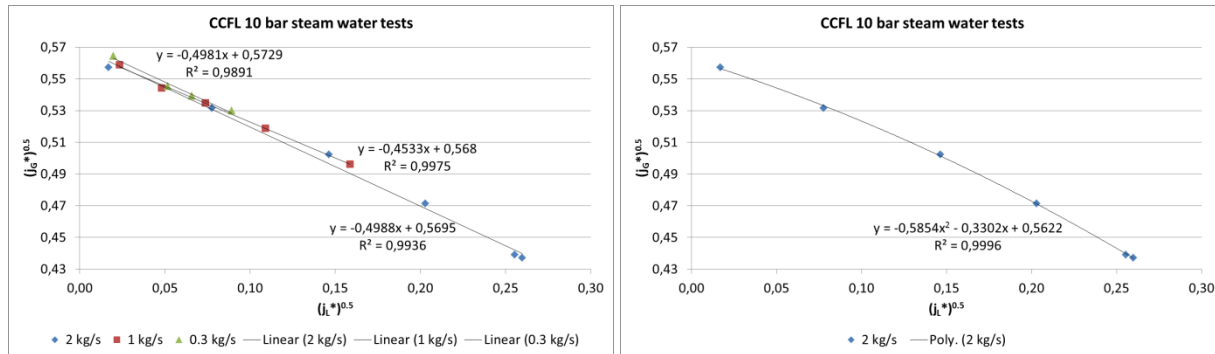


Fig. 9 Analysis of the flooding characteristics for the 10 bar tests; left: series for all injected liquid mass flows with linear fits; right: quadratic approximation of the 2 kg/s series

Tab. 3 Parameter of the flooding curve analysis

Pressure [bar]	Injected liquid mass flow [kg/s]	P2	P1	P0	$R^2$
1	2		-0.6074	0.5522	0.9965
		-0.1273	-0.5666	0.5502	0.9967
1	1		-0.5821	0.5526	0,9881
1	0.3		-0.4660	0.5455	0,9240
2	2		-0.6565	0.5703	0.9987
		-0.0874	-0.6313	0.5711	0.9987
2	1		-0.6244	0.5703	0,9978
10	2		-0.4988	0.5695	0.9936
		-0.5854	-0.3302	0.5622	0.9996
10	1		-0.4533	0.5680	0,9975
10	0.3		-0.4981	0.5729	0,9891
25	2		-0.5518	0.5972	0.9929
		-0.5555	-0.3765	0.5882	0.9985
25	1		-0.4572	0.5860	0,9997
25	0.3		-0.4511	0.5878	0,9991
50	2		-0.5751	0.6150	0.9882
		-0.8817	-0.2164	0.5859	0.9993
50	1		-0.4816	0.6031	0,9998

Although the injected liquid flow rate seems to have only minor influence on the flooding characteristics (see Fig. 8) there is a trend that the slope  $P1$  of the linear fits slightly increases for fixed pressure with the injected liquid flow rate. The only exception is the test series at 10 bar and 0.3 kg/s injected water mass flow rate. Here some uncertainties in the fitting may arise from the fact that only few measurement points are available for this test series. The comparison of the slopes between the different pressure levels under consideration of constant injected liquid mass flow shows a decrease with increasing pressure if air-water and steam-water is considered separately. The slope for air-water test series is generally larger than for steam-water tests. The slope coefficients in dependence on the pressure are shown on the left side of Fig. 10. The analysis of the single slope values reveals, that especially for the series with 0.3 kg/s water injection they deviate from the 1 and 2 kg/s measurements. The accuracy of this parameter depends on the number and on the range of the data. So for this analysis the 0.3 kg/s series were excluded and in this plot are presented averaged values of the linear fits of the 1 and 2 kg/s tests.

The absolute coefficient  $P0$  represents the intersection with the ordinate. For the flooding characteristics this point can be interpreted as zero penetration value. The  $P0$  values for the linear fit for 1 kg/s and for the quadratic approximation in the 2 kg/s case are almost the same. Accordingly they are averaged for the presentation on the right side of Fig. 10. Also in this plot the 0,3 kg/s coefficients were excluded for the aforementioned reasons. The resulting zero penetration points slightly increase with increasing pressure, if air and steam are considered individually.

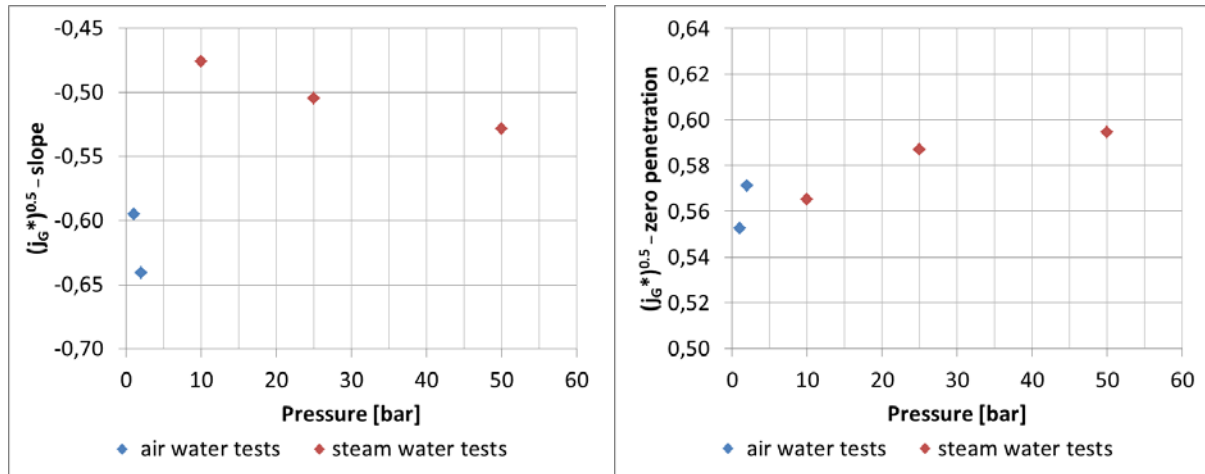


Fig. 10 Plot of the slope (left hand side) and the zero penetration (right hand side) coefficients as function of the pressure

The calculated zero penetration points  $P_0$  are also shown as vertical lines in Fig. 7. All series except the case 2 bar and 1 kg/s satisfy the condition that the experimental gas flow rate for zero penetration was larger than or equal to the calculated values  $P_0$ . Also the experimental CCFL points near zero condition are always lower than the calculated zero value. This demonstrates the consistency of the data verifies of zero penetration condition from the visual observation.

As described above slug frequencies were obtained by a FFT from the pressure sensors at the horizontal part of the hot leg. These frequencies are plotted in Fig. 11 for all test points at which slugs appeared, i.e. for all test points with CCFL and excluding the measurements for unlimited counter-current flow. For clarity the points are also arranged by test series and labeled by the same symbols and colors as in Fig. 8. The plot reveals two clear trends: On the one hand it is obvious, that the slug frequency by trend increase with increasing pressure and on the other hand the slug frequency decreases with increasing injected water mass flow, if the pressure is kept constant.

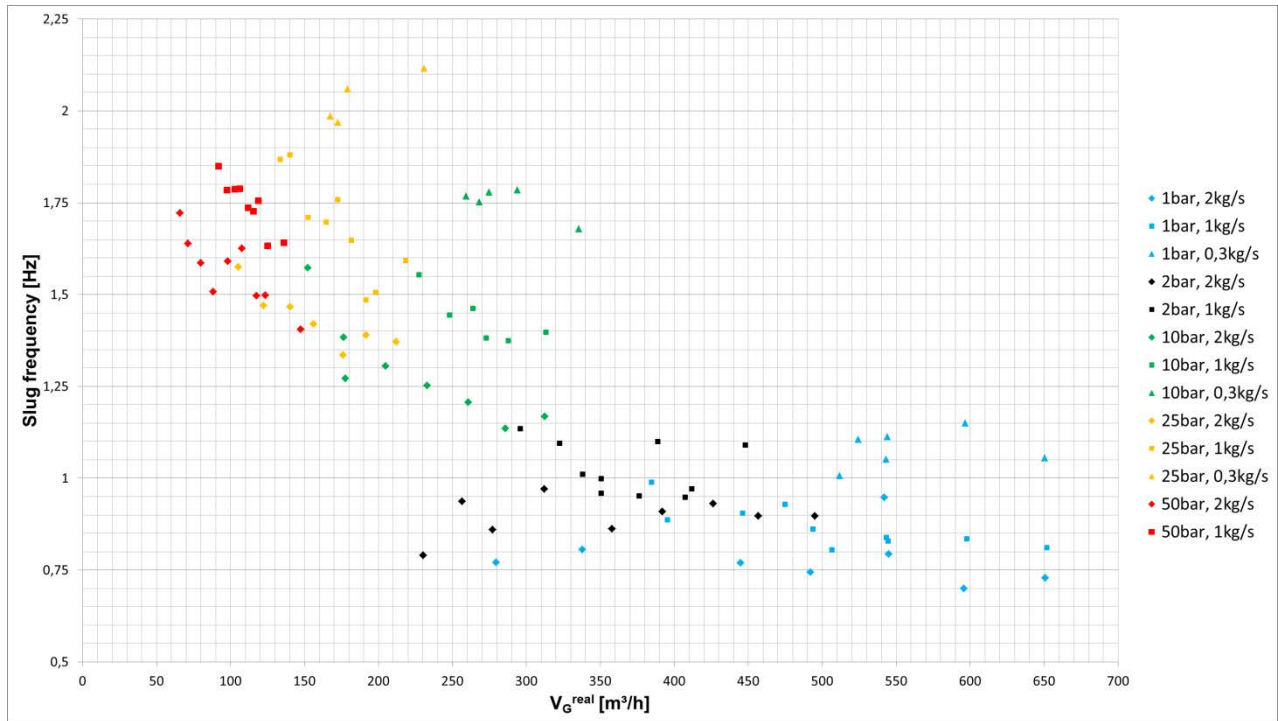


Fig. 11 Visualization of the averaged slug frequencies as function of the real gas volume flow, sorted by test series

Generally the dependence of slug frequencies on the gas flow rate is low. For some pressure levels the slug frequency slightly decreases with increasing gas flow. This effect is visible for 10 bar (2, 1 and 0.3 kg/s), for 25 bar (2 and 1 kg/s) and for 50 bar (2 and 1 kg/s). However the air test series and the 25 bar 0.3 kg/s test series doesn't follow this trend. In consideration of the wide frequency spectrum for the single tests this effect may be inside the measurement and evaluation uncertainty.

For this reason slug frequencies averaged over a single test series are shown in Fig. 12. These data confirm the above mentioned trends on the increase of the slug frequency with pressure and the decrease with increasing injected water flow rate.

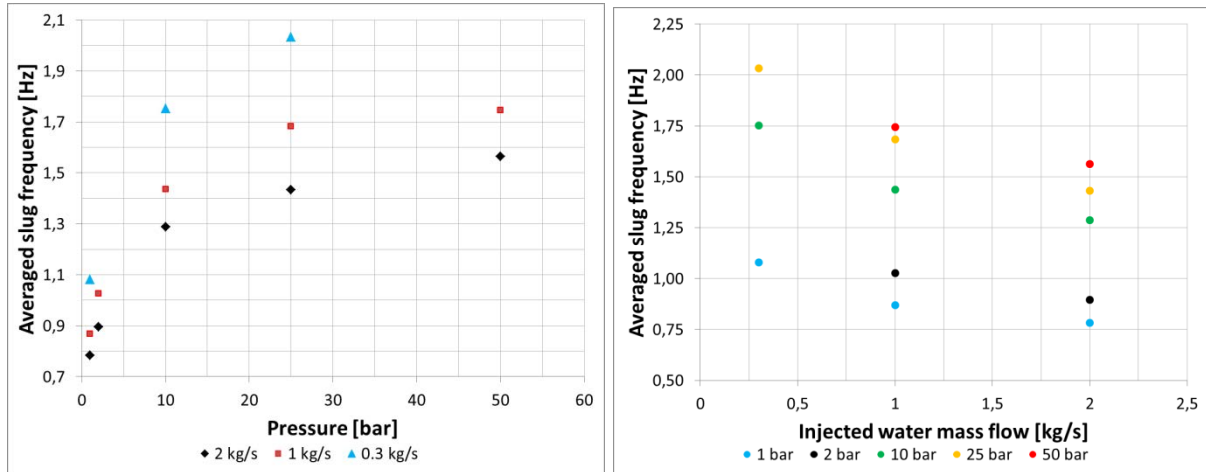


Fig. 12 Slug frequencies averaged over the single test series in dependence on pressure and injected water mass flow rate

As mentioned above the flow structure was recorded by 3 video cameras. Accordingly comprehensive video material is available. Up to now it was only used for a qualitative assessment of the flow. It is planned to extract more quantitative data for CFD model development and validation by appropriate image processing procedures in future.

Fig. 13 shows some exemplary pictures from the high-speed video camera data for the SG inlet chamber module for the test series 50 bar and 1 kg/s injected water flow rate and Fig. 14 both sections of the horizontal part of the hot leg for test series 50 bar and 2 kg/s. The process starts with an unhindered flow from the SG separator to the RPV simulator tank. (test 180 for Fig. 13 left hand side and test 160 for Fig. 14 top). With increasing gas flow rate the CCFL started in the horizontal test section part. The flow was wavier with an increasing level in the horizontal part from the RPV side to the SG side. Near the transition to the inclined part first slugs appeared, but they didn't touch the top wall (central pictures in Figs. 13 and 14, tests 181 and 161 respectively). A further increase of the gas flow led to an intensification of the water obstruction and to a rise of the slug level up to the top wall. The gas flow pushed the slugs into the inclined part and further over the steel sheet between B20A and B20B. In this way the discharge water flow decreased down to zero, if the gas flow is high enough (right picture in Fig. 13 and bottom picture in Fig. 14). During zero penetration the horizontal channel on the RPV

side is partly waterless (see Fig. 14 bottom, left), at which the border moves along the RPV faced horizontal channel module. A decreasing gas flow led to a reverse process with a hydraulic jump that moved from the RPV faced horizontal channel into the inclined module.

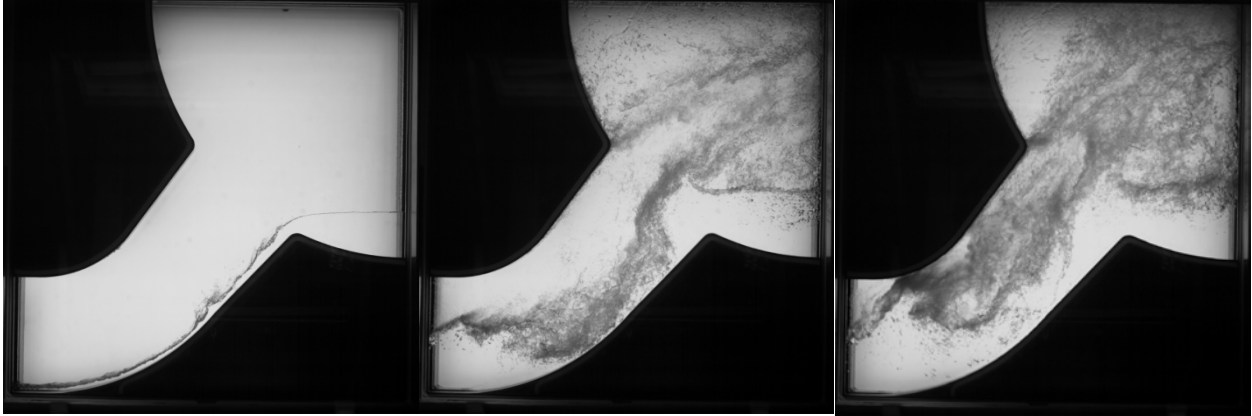


Fig. 13 Pictures from the high-speed video camera observations of the SG inlet chamber module: left test 180, middle test 181, right test 184

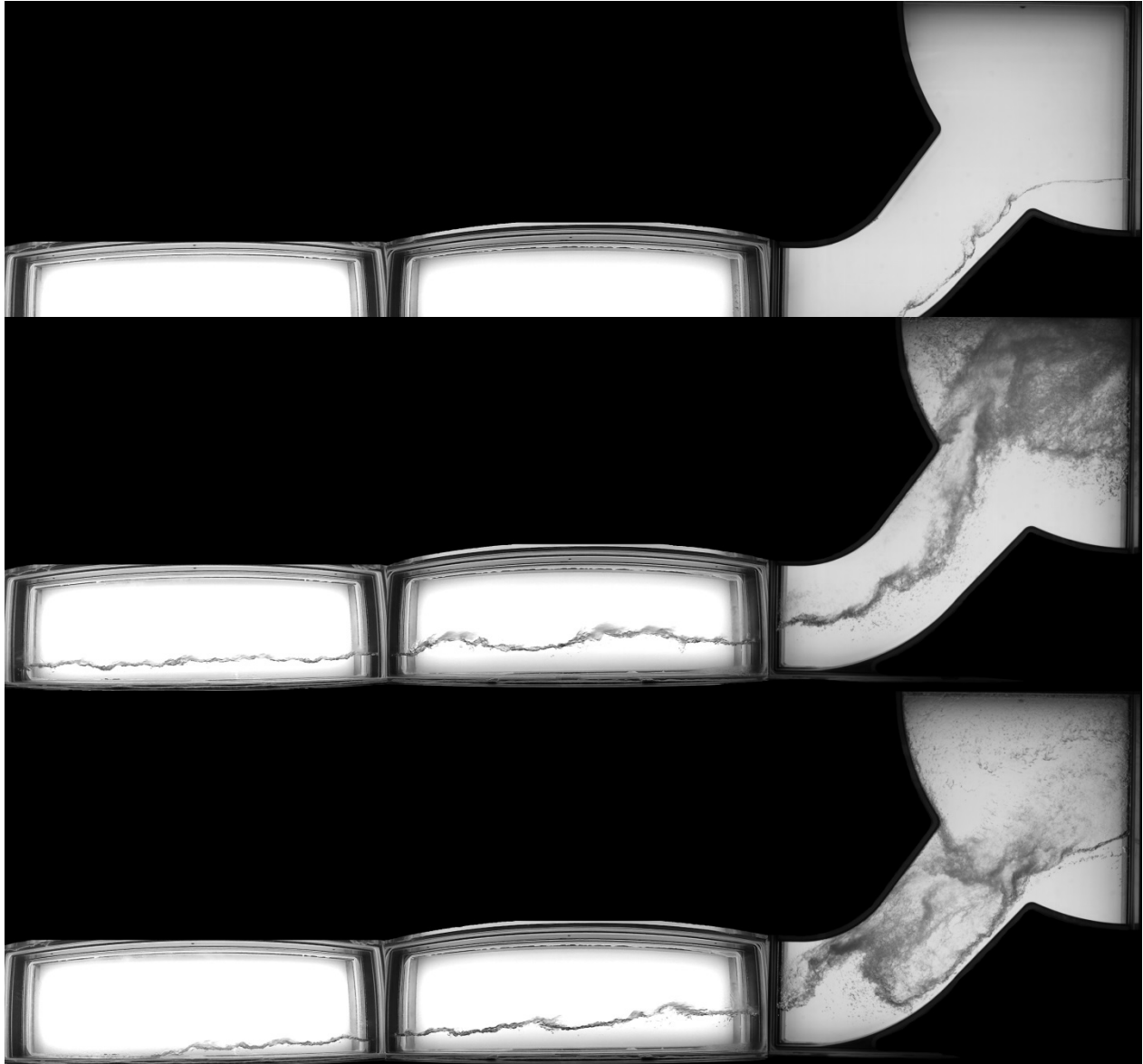


Fig. 14 Pictures from the web cam observations of the horizontal part of the hot leg: top test 160, middle test 161, bottom test 162

#### 4. Summary

The flooding characteristics were measured in a flat model of a PWR hot leg including a part of the SG inlet chamber. Experiments were done in the same test section for air-water flows at 1 and 2 bar as well as for steam-water flows at 10, 25 and 50 bar. The

steady state of the CCFL situation allowed to obtain more consistent flooding characteristics as obtained in previous transient experiments.

The flooding curves show a slight, but very clear dependency on pressure when they are presented in terms of the dimensionless Wallis parameters. For the same dimensionless discharged water flow rates the dimensionless gas flow rates increase with pressure. That means that during partial CCFL more water can flow in counter-current to a constant gas flow rates in case of increased pressure. Furthermore the dimensionless gas flow rates for zero penetration also slightly increase with pressure. A clear hysteresis was observed between onset of flooding and breakdown of flooding.

An analysis of the slug frequencies showed that they increase with pressure and decrease with the injected air flow rate.

Details of the flow structure can be extracted from the comprehensive video material which was obtained in the measurements. This has to be done in future to obtain additional data for CFD code qualification.

## **Acknowledgements**

This work is carried out in the frame of a research project funded by the German Federal Ministry of Economic Affairs and Energy, project number 150 1411.

## **References**

Al Issa, S., and Macian, R., 2011. A Review of CCFL Phenomena. *Ann. Nucl. Energy*, 38, 1795.

Al Issa, S., and Macian, R., 2014. Experimental Investigation of Countercurrent Flow Limitation (CCFL) in a Large-Diameter Hot-Leg Geometry: A Detailed Description of CCFL Mechanisms, Flow Patterns and High-quality HSC Imaging of the Interfacial

Structure in a 1/3.9 Scale of PWR Geometry. *Nuclear Engineering and Design*, 280, 550–563.

Bankoff, S.G., Lee, S.C., 1986. A critical review of the flooding literature. *Multiphase Science and Technology* 2, 95-180.

Beyer, M., Lucas, D., Pietruske, H., Szalinski, L., 2016. Two-Phase Flow Experiments on Counter-Current Flow Limitation in a model of the Hot Leg of a Pressurized Water Reactor (2015 test series). *Wissenschaftlich-Technische Berichte des Helmholtz-Zentrums Dresden – Rossendorf, HZDR-076, ISSN 2191-8716.*

Deendarlianto, Vallée, C., Lucas, D., Beyer, M., Pietruske, H., Carl, H., 2011. Experimental study on the air/water counter-current flow limitation in a model of the hot leg of a pressurised water reactor. *Nuclear Engineering and Design* 241, 3359–3372.

Deendarlianto, Höhne, T., Lucas, D., Vallée, C., Montoya, G., 2011. CFD studies on the phenomena around counter-current flow limitations of gas/liquid two-phase flow in a model of a PWR hot leg. *Nuclear Engineering and Design* 241, 5138-5148.

Deendarlianto; Höhne, T., Murase, M., 2012. Countercurrent flow limitations in a pressurized water reactor. *Science and Technology of Nuclear Installations*, 608678.

Jeong, H.Y., 2002. Prediction of counter-current flow limitation at hot leg pipe during a small-break LOCA. *Annals of Nuclear Energy* 29 (5), 571–583.

Kinoshita, I., Murase, M., Utanohara, Y., Lucas, D., Vallée, C., Tomiyama, A., 2012. Numerical calculations for steam-water CCFL tests using the 1/3rd scale rectangular channel simulating a PWR hot leg. *Nuclear Engineering and Design* 249, 14-23.

Kinoshita, I., Murase, M., Yoichi, U., Lucas, D., Vallée, C., Tomiyama, A., 2014. Effects of shape and size on countercurrent flow limitation in flow channels simulating a PWR hot leg. *Nuclear Technology* 187 (1), 44-56.

Lucas, D., Rzehak, R., Krepper, E., Ziegenhein, Th.; Liao, Y., Kriebitzsch, S., Apanasevich, P., 2016. A strategy for the qualification of multi-fluid approaches for nuclear reactor safety. *Nuclear Engineering and Design* 299, 2-11.

Minami, N., Nishiwaki, D., Kataoka, H., Tomiyama, A., Hosokawa, S., Murase, M., 2008. Experiments on air-water countercurrent flow in a rectangular duct simulating PWR hot leg. In: *Proceedings of the 16th International Conference on Nuclear Engineering*, Orlando (FL), USA, May 11–15 (Article No. ICONE16-48113).

Nariai, T., Tomiyama, A., Vallée, C., Lucas, D., Kinoshita, I., Murase, M., 2010. Countercurrent flow limitation in a scale-down model of a PWR hot leg. *The 8th International Topical Meeting on Nuclear Thermal-Hydraulics, Operation and Safety (NUTHOS-8)*, 10.-14.10.2010, Shanghai, China, paper N8P0109.

Ohnuki, A., 1986. Experimental study of counter-current two-phase flow in horizontal tube connected to inclined riser. *Journal of Nuclear Science and Technology* 23 (3), 219–232.

Ohnuki, A., Adachi, H., Murao, Y., 1988. Scale effects on countercurrent gas-liquid flow in a horizontal tube connected to an inclined riser. *Nuclear Engineering and Design* 107 (3), 283–294.

Richter, H.J., Wallis, G.B., Carter, K.H., Murphy, S.L., 1978. Deentrainment and counter-current air-water flow in a model PWR hot leg. *U.S. Nuclear Regulatory Commission Report No. NRC-0193-9*, Hanover (NH), USA.

Vallée, C., Seidel, T., Lucas, D., Beyer, M., Prasser, H.-M., Pietruske, H., Schütz, P., Carl, H., 2012. Counter-current flow limitation in a model of the hot leg of a PWR - comparison between air/water and steam/water experiments. *Nuclear Engineering and Design* 245, 113-124.

Wallis, G.B., Dobson, J. E., 1973. The onset of slugging in horizontal stratified air-water flow, *International Journal of Multiphase Flow* 1, 173 – 193.

Wang M.J., Mayinger, F., 1995. Simulation and analysis of thermal-hydraulic phenomena in a PWR hot leg related to SBLOCA. *Nuclear Engineering and Design* 155, 643-652.

Weiss, P.A., Hertlein, R.J., 1988. UPTF test results: first three separate effect tests. *Nuclear Engineering and Design* 108 (1–2), 249–263.

Wongwises, S., 1996. Two-phase countercurrent flow in a model of a pressurized water reactor hot leg. *Nuclear Engineering and Design* 166, 121-133.